

RAD: Retrieval-Augmented Monocular Metric Depth Estimation for Underrepresented Classes

Michael Baltaxe^{1,2} Dan Levi¹ Sagie Benaim²

¹General Motors, Herzliya, Israel

²The Hebrew University of Jerusalem, Jerusalem, Israel

Abstract

Monocular Metric Depth Estimation (MMDE) is essential for physically intelligent systems, yet accurate depth estimation for underrepresented classes in complex scenes remains a persistent challenge. To address this, we propose RAD, a retrieval-augmented framework that approximates the benefits of multi-view stereo by utilizing retrieved neighbors as structural geometric proxies. Our method first employs an uncertainty-aware retrieval mechanism to identify low-confidence regions in the input and retrieve RGB-D context samples containing semantically similar content. We then process both the input and retrieved context via a dual-stream network and fuse them using a matched cross-attention module, which transfers geometric information only at reliable point correspondences. Evaluations on NYU Depth v2, KITTI, and Cityscapes demonstrate that RAD significantly outperforms state-of-the-art baselines on underrepresented classes, reducing relative absolute error by 29.2% on NYU Depth v2, 13.3% on KITTI, and 7.2% on Cityscapes, while maintaining competitive performance on standard in-domain benchmarks.

1. Introduction

Monocular metric depth estimation (MMDE) is crucial to building intelligent systems and immersive digital experiences that interact with the physical world. Applications span autonomous driving [50], human-computer interaction [9, 12], and novel view synthesis [20]. Given the long-tailed nature of real-world data, accurately estimating depth for underrepresented classes is essential for their robust deployment. In this work, we address MMDE in complex scenes that contain long-tailed, underrepresented classes.

Recent years have seen substantial progress in MMDE. Two prevailing directions have been investigated, depending on the type of data available for the task. One set of approaches relies on using domain-specific data to fine-

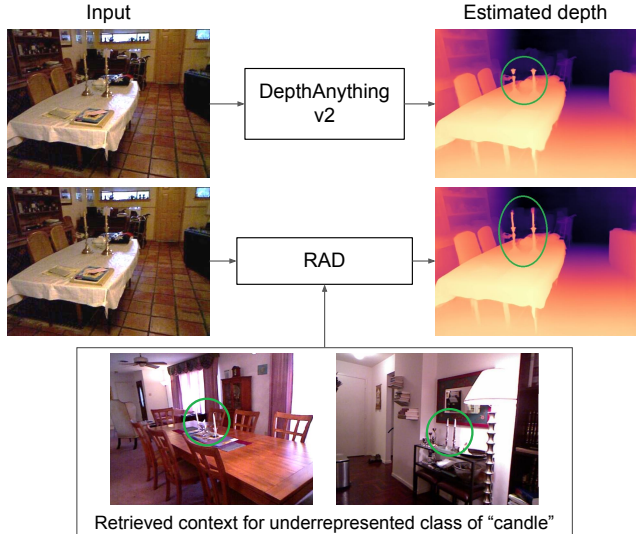


Figure 1. **Illustration.** Given an input image, RAD (using DepthAnything v2 backbone [53]) retrieves context views for highly uncertain objects of underrepresented classes (e.g., candles) to serve as structural geometric proxies. These are used as part of a dual-stream network to output an accurate monocular metric depth estimation, in comparison to the direct baseline of DepthAnything v2, fixing uncertain regions.

tune depth estimation networks that incorporate strong priors [2, 13, 45, 57]. These methods aim for specialization, resulting in networks that accurately estimate depth when trained with sufficient representative data. The second set of approaches learns from several large-scale datasets to perform zero-shot MMDE [4, 5, 18, 39], which aims for strong generalization, enabling the model to perform well on unseen target domains without test-time adaptation. Although promising, key gaps persist. On the one hand, fine-tuning methods yield highly accurate estimates for in-distribution classes, but when presented with underrepresented classes, the priors are inaccurate, leading to large errors. On the other hand, zero-shot methods ignore domain-specific information, resulting in a performance degradation.

It is well established that multi-view methods outperform monocular depth estimation due to their incorporation of geometric constraints from multiple viewpoints. Such additional information helps mitigate the limitations inherent to monocular setups. Our approach, called RAD (standing for Retrieval Augmented Depth), remains within the monocular estimation framework but seeks to approximate the benefits of multi-view systems by retrieving content-relevant images that serve as proxy auxiliary supporting views for the input (see Fig. 1). To this end, we draw inspiration from the retrieval-augmented generation (RAG) paradigm [31], used in vision and language tasks.

Our training procedure for RAD consists of three main stages. First, we source a context sample, which consists of a context image (RGB) and its corresponding ground-truth depth map (D). This sample is generated in one of two ways: (a) via our uncertainty-aware retrieval pipeline, which uses the baseline’s uncertainty to find a similar context image, or (b) via 3D augmentation, which generates a new image and depth map from a random viewpoint. Second, we establish spatial correspondences between the input image and the sourced context image (for retrieved images, this is done via point matching; for 3D augmentations, these correspondences are known via the geometry). Finally, the complete context sample (RGB+D) is processed by our dual-stream network, which uses a matched cross-attention mechanism to fuse the context information only at these corresponding locations. At inference, we follow the same procedure as in training, with the exception that context images are only obtained using our uncertainty-aware retrieval pipeline.

We demonstrate that RAD delivers substantial gains over state-of-the-art MMDE methods in regions containing underrepresented classes, while maintaining or even enhancing performance in in-domain regions. To validate this, we evaluate RAD across both underrepresented and in-domain categories in complex scenes, comparing against fine-tuning and zero-shot baselines on NYU Depth v2 [46], KITTI [15], and Cityscapes [7]. To enable a robust evaluation on underrepresented classes, we introduce a new benchmark depicting underrepresented classes from each of these datasets. On underrepresented classes, our method achieves relative improvements in absolute relative error of 29.2%, 13.3%, and 7.2% on NYU, KITTI, and Cityscapes, respectively. For in-domain classes, RAD matches or even improves upon existing methods without degradation.

2. Related Work

Supervised Monocular Depth Estimation. Most monocular depth estimation approaches rely on fully annotated datasets. Early work [11, 29] showed that depth can be directly regressed from ground truth and introduced loss functions to address scale ambiguity. This paradigm has evolved through improved regression techniques [13, 43],

depth distribution modeling [2, 3, 45], and global scene consistency enforcement [57], resulting in highly accurate methods. While supervised models learn strong priors from large datasets, they struggle to generalize to long-tail regions, precisely the focus of our work.

Self-supervised Monocular Depth Estimation. Due to the data demands of fully supervised methods, self-supervised approaches have emerged as an alternative. These typically use video sequences, multi-camera setups, or auxiliary signals, paired with loss functions enforcing color constancy to enable monocular depth estimation [16, 17, 40, 49, 60]. Like supervised methods, they rely on large datasets to learn strong priors and struggle with underrepresented data. Our retrieval mechanism addresses this by explicitly sourcing relevant context.

Domain Adaptation for Monocular Depth Estimation. Domain adaptation for monocular depth estimation addresses the shift between labeled source and unlabeled target domains [1, 34, 59]. While it bridges cross-domain gaps, our work focuses on intra-domain imbalance caused by long-tailed data distributions.

Zero-shot and Few-shot Monocular Depth Estimation. Recent zero-shot methods use massive datasets to enable broad generalization. These approaches have progressed from estimating relative depth [10, 27, 42, 53, 55], to recovering metric scale via camera intrinsics [4, 18, 22, 38, 56], and more recently, to jointly estimating depth and camera parameters [5, 39]. [23] proposed a few-shot method to adapt to new distributions using minimal labeled data. Unlike our approach, both paradigms trade domain-specific precision for generality, often degrading performance on complex, underrepresented classes where local priors are crucial.

Retrieval for Monocular Depth Estimation. While [26] introduced non-parametric retrieval with costly test-time optimization, we present the first deep, parametric, feed-forward retrieval-augmented framework. Unlike multi-view methods [14, 32, 35, 52] that fuse views of the *same* scene, our approach retrieves *semantically similar* in-the-wild images to enhance single-image depth estimation.

OOD and Open-Set 3D Vision. Most out-of-distribution (OOD) approaches in 3D vision focus on *anomaly detection* [21, 24, 28, 47, 48, 58]. Recent open-set methods use deep visual [6, 19] and textual encodings [54], but remain limited to detection and classification. In contrast, we tackle *metric depth estimation*, using retrieved priors to reconstruct geometry for underrepresented data, not just detect it.

3. Method

We now describe our method. First, we detail the *training procedure* in Sec. 3.1. During training, context images and corresponding depth maps are sourced either by retrieving samples containing similar underrepresented classes or

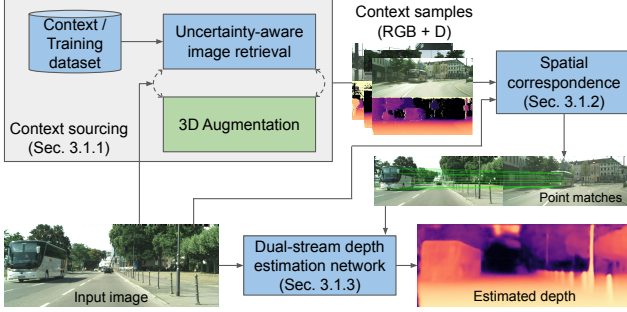


Figure 2. **RAD Pipeline.** Given an input image, a set of context samples is sourced (Sec. 3.1.2) using either *uncertainty aware image retrieval* (both at training and inference) or *3D augmentation* (only during training). Subsequently, spatial correspondences are established (Sec. 3.1.2). These are used to infer depth via a dual-stream depth estimation network employing *matched cross-attention* (Sec. 3.1.3). Blue blocks indicate components used for training and inference, while the green block is only for training.

via 3D augmentation of the input image (Sec. 3.1.1). We then establish spatial correspondences between the input and context images (Sec. 3.1.2) to guide matched cross-attention within a dual-stream network that performs depth estimation (Sec. 3.1.3). Second, we describe the *inference procedure* in Sec. 3.2. This follows the same pipeline as training, except that context is sourced exclusively via retrieval. Fig. 2 presents an overview of RAD.

3.1. Training

3.1.1. Context Sourcing

Let $T = \{(x_i, d_i)\}_{i=1}^N$ be the training dataset, where each x_i is an input image and d_i its corresponding ground-truth depth map. For each sample $(x_t, d_t) \in T$, we construct a context $C = \{(x_c^i, d_c^i)\}_{i=1}^M$, consisting of M context images x_c^i and their associated depth maps d_c^i . For a given train sample $(x_t, d_t) \in T$, the context C is generated using one of two randomly selected procedures: (1) uncertainty-aware image retrieval or (2) 3D augmentation, as detailed below.

Uncertainty-aware Image Retrieval. Let $D_{pool} = \{(x_i, d_i)\}_{i=1}^L$ denote the context dataset from which context samples are retrieved, where x_i represents an image and d_i its corresponding ground-truth depth map (in our setting, we use the training set for D_{pool} , i.e., $D_{pool} = T$). Given a training sample $(x_t, d_t) \in T$, our objective is to retrieve a subset of M context samples, $C \subseteq D_{pool}$ (from different scenes than that of (x_t, d_t)), such that images in C contain objects similar to those underrepresented objects in x_t .

Conventional retrieval methods based on image descriptors tend to favor images with similar scene layouts. To address this limitation, we propose a custom retrieval strategy. Our central insight is that a depth estimation network trained on a dataset with representative distributions exhibits elevated uncertainty when encountering underrep-

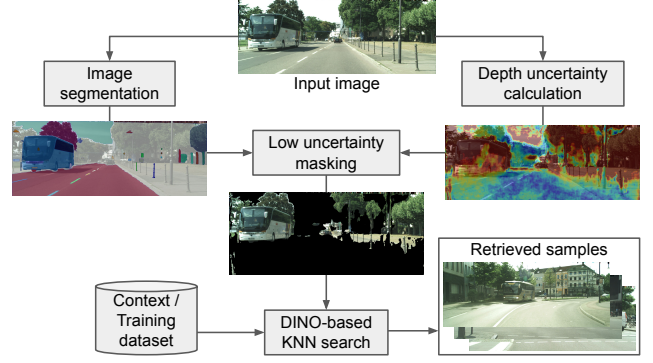


Figure 3. **Uncertainty-aware retrieval flow.** Pixel-wise depth uncertainty is calculated in parallel to image segmentation. We use these to keep only highly uncertain segments, masking the rest of the image. Given the masked image we retrieve relevant examples from the context/training set using DINO descriptors.

resented object classes. This phenomenon arises from the weak priors encoded in the network’s parameters due to insufficient training data. We leverage this uncertainty signal to identify underrepresented objects within an image and guide the retrieval of relevant samples. Fig. 3 illustrates the proposed uncertainty-aware retrieval pipeline.

Following the methodology outlined in [41], pixel-wise uncertainty is estimated by training a depth estimation network D on a representative dataset, applying it multiple times to perturbed versions of the input image, and analyzing the resulting standard deviation. Let x_t denote the training image, and let $N(x_t)$ represent a noisy variant of x_t , generated by injecting random Gaussian noise, with standard deviation σ . Let $D(y)$ denote the estimated depth for some image y , calculated by a frozen version of a depth estimation model that uses our backbone. Define $\text{std}(X)$ as the pixel-wise standard deviation and $\mathbb{E}(X)$ as the pixel-wise mean of a set of images X . The pixel-wise uncertainty for x_t , denoted $\text{Uncertainty}(x_t)$, is computed as follows:

$$\text{Noisy}(x_t) = \{N(x_t)\}_{i=1}^n \quad (1)$$

$$\text{Uncertainty}(x_t) = \frac{\text{std}(\{D(y) \mid y \in \text{Noisy}(x_t)\})}{\mathbb{E}(\{D(y) \mid y \in \text{Noisy}(x_t)\})}. \quad (2)$$

Given a training sample $(x_t, d_t) \in T$, we first compute $U = \text{Uncertainty}(x_t)$ using DepthAnything v2 [53] for $D(\cdot)$, and generate a segmentation map $S = \text{Segmentation}(x_t)$ using SAM2 [44]. For each segment $s \in S$, we compute the number of pixels exceeding a predefined uncertainty threshold h : $p(s, U, h) = |\{x \mid x \in s \wedge U(x) > h\}|$.

To isolate regions of high uncertainty, we retain only segments $s \in S$ for which at least $q\%$ of pixels exceed thresh-

old h . Thus, we generate a masked image \tilde{x}_t , as follows:

$$Keep(U, S, q, h) = \{s \in S \mid p(s, U, h) > \frac{|s| \cdot q}{100}\} \quad (3)$$

$$\tilde{x}_t(x) = \begin{cases} x_t(x), & \exists s \in Keep(U, S, q, h), \text{s.t. } x \in s \\ 0, & \text{otherwise.} \end{cases} \quad (4)$$

Finally, let $\text{DINO}(x)$ represent the DINO v2 descriptor [36] of image x , and define $\text{KNN}(x, Y, M)$ as the set of M nearest neighbors to descriptor x within the descriptor set Y . Then, the uncertainty-aware retrieved context C is:

$$\text{DINO}_{D_{pool}} = \{\text{DINO}(x) \mid (x, d) \in D_{pool}\} \quad (5)$$

$$W = \text{KNN}(\text{DINO}(\tilde{x}_t), \text{DINO}_{D_{pool}}, M) \quad (6)$$

$$C = \{c \in D_{pool} \mid \text{DINO}(c) \in W\}. \quad (7)$$

In our implementation, cosine similarity is used to compute nearest neighbors. In effect, we use a masked image as query to retrieve from a pool of non-masked images. Empirically, this showed to be viable as the DINO v2 embedding aggregates a thorough description of the image contents.

3D Augmentation. Training using only retrieved samples from a fixed context dataset leads to repetitive context for each training image across epochs. To promote robustness to varying contexts, we use a 3D augmentation method.

To promote robustness to varying contexts, we employ a 3D augmentation strategy. Given a training sample $(x_t, d_t) \in T$ and camera intrinsics K , we generate a synthetic context set $C = \{(x_c^i, d_c^i)\}_{i=1}^M$. We first back-project the input image to 3D points $X = \text{Backproj}(x_t, d_t, K)$. Then, we sample M random camera poses $\{[R_i | t_i]\}_{i=1}^M$ and render the scene from these new viewpoints to obtain $x_c^i = \text{Proj}(X, K, [R_i | t_i])$ and $d_c^i = Z(X, K, [R_i | t_i])$, where Proj and Z denote the image and depth projection functions respectively. To avoid holes when projecting from a new point of view, we create a mesh (see supplementary).

3.1.2. Spatial Correspondence

Once training sample $(x_t, d_t) \in T$ is complemented with context C , we search for precise spatial correspondences.

When uncertainty-aware retrieval is used, we apply an off-the-shelf point matching method to identify semantic correspondences between training image x_t and context images $\{x_c^i\}_{i=1}^M$. Specifically, we use LightGlue [33], which efficiently detects matches. When 3D augmentation is used, correspondences are calculated analytically through projective geometry. These correspondences then guide cross-attention at matched locations, as detailed next in Sec. 3.1.3.

3.1.3. Dual-stream Depth Estimation Network

Our network builds upon the DepthAnything v2 architecture [53], utilizing the same Vision Transformer (ViT) encoder and DPT decoder [43] for dense depth estimation.

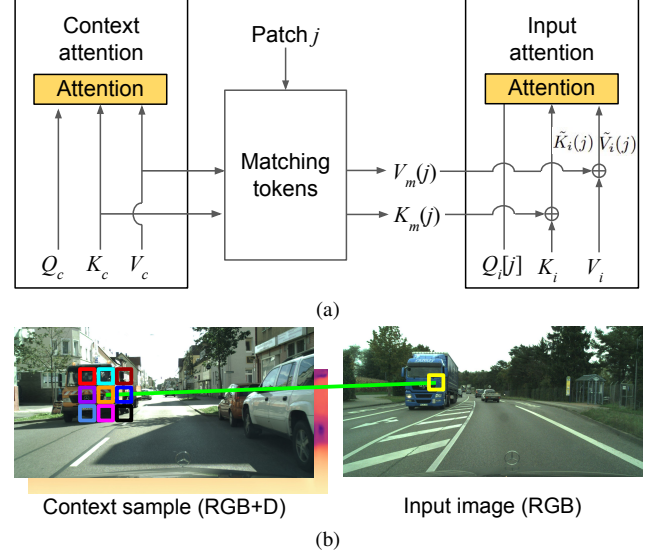


Figure 4. **Matched Cross-Attention.** (a) illustrates the modified attention architecture designed to enable effective information transfer from the context stream to the input stream. For each token j in the input image, with query vector $Q_i[j]$, attention is computed using key and value matrices formed by concatenating the input’s keys (K_i) and values (V_i) with the matched context keys ($K_m(j)$) and values ($V_m(j)$). These matched matrices are constructed by selecting j ’s matching context tokens from the full context matrices K_c and V_c , respectively. (b) shows that matching tokens are defined as those located within a spatial neighborhood surrounding the matched point of j in the context image.

The network is formed by two parallel ViT encoders, one for the RGB input and one for the RGB+D context sample. To incorporate depth into the context stream, a fourth channel is added to the projection operation at the beginning of its ViT encoder. Let $(x_c, d_c) \in C$ be a context sample, with $x_c \in \mathbb{R}^{H \times W \times 3}$ and $d_c \in \mathbb{R}^{H \times W \times 1}$, where W and H are the image’s width and height, respectively. The projection operation in the context stream is defined as a function $P : \mathbb{R}^{H \times W \times 4} \rightarrow \mathbb{R}^{H_P \times W_P \times c}$, where $H_P \times W_P$ are the number of patches extracted, and c is the dimensionality of the projected patch embeddings. The input to P is constructed by concatenating x_c and d_c along the channel axis, yielding the projected representation $P(\text{concat}(x_c, d_c))$.

The input and context streams are linked via cross-attention at matching points. The context stream processes tokens using standard self-attention, while the input stream integrates information from the context stream through matched cross-attention detailed below. The architecture for both streams is the same as DepthAnything v2, except for the context encoder adaptation described above and the attention mechanism in each block of the input stream. Both streams run in parallel. Our training objectives are identical to DepthAnything v2, aiming to predict the depth of the input stream. Note that these design choices

are general, making our method easily adaptable to different backbones and objectives. The overall network architecture, training and implementation details, as well as memory and inference-time analysis, are provided in the supplementary.

Matched Cross-Attention. To enable effective information exchange between the context and input streams, we propose a modified attention mechanism called *matched cross-attention*. As depicted in Fig. 4(a), this mechanism allows the input stream to integrate contextual information by augmenting its attention computation as follows.

Let Q_i , K_i , and V_i be the queries, keys, and values matrices for the input feature map, where j represents the position of a given token in this feature map. Likewise, let Q_c , K_c and V_c be the queries, keys, and values matrices for the corresponding context feature map. For any of the matrices X defined above, by $X[a]$ we refer to the vector in X corresponding to token a . Additionally, let $\text{matching_tokens}(j)$ represent the set of context tokens matched to token corresponding to j in the input image. Then, the attention for token j in the input feature map, denoted A_j , is:

$$K_m(j) = \{K_c[a] \mid a \in \text{matching_tokens}(j)\} \quad (8)$$

$$V_m(j) = \{V_c[a] \mid a \in \text{matching_tokens}(j)\} \quad (9)$$

$$\tilde{K}_i(j) = \text{concat}(K_i, K_m(j)) \quad (10)$$

$$\tilde{V}_i(j) = \text{concat}(V_i, V_m(j)) \quad (11)$$

$$A_j = \text{attention}(Q_i[j], \tilde{K}_i(j), \tilde{V}_i(j)) \quad (12)$$

where attention is the standard attention mechanism.

As illustrated in Fig. 4(b), the matching tokens associated with token j are defined as those located within a spatial neighborhood surrounding its matched point in the context sample. This approach preserves spatial locality while facilitating cross-image correspondence. If more than one image is retrieved, we aggregate context tokens through all of them. Importantly, the set $\text{matching_tokens}(j)$ varies for each input token j , resulting in distinct key and value matrices for each attention computation.

3.2. Inference

At inference time, given an input image I , RAD employs uncertainty-aware retrieval to assemble context $C = \{(x_c^i, d_c^i)\}_{i=1}^M$, as defined in Eq. 7 (Sec. 3.1.1). Then, point correspondences between I and the retrieved context images $\{x_c^i\}_{i=1}^M$ are computed following the procedure outlined in Sec. 3.1.2. Finally, depth estimation is performed using the network described in Sec. 3.1.3, incorporating matched cross-attention as detailed in Eq. 12.

4. Experiments

We demonstrate the effectiveness of RAD through quantitative and qualitative evaluations. We stress that in all experiments, our retrieval context dataset D_{pool} is from the

training set, making comparison to baselines fair. We then conduct experiments to visualize and analyze the behavior of RAD’s core components. Finally, we present a series of ablation studies. Limitations are in the supplementary.

4.1. Experimental Setup

Datasets. We evaluate our method on three widely used depth estimation datasets: NYU Depth v2 [46], KITTI [15] (Eigen split), and Cityscapes [7]. Since our focus is on underrepresented classes, we use semantic segmentation annotations to determine the location of underrepresented classes (detailed below) in test images, and calculate metrics (detailed below) on pixels of such classes in an isolated manner. Both NYU and Cityscapes provide ground-truth semantic segmentation annotations (for Cityscapes, we use the fine annotations from the validation split). KITTI, however, lacks semantic labels (a limitation that motivates the inclusion of Cityscapes as an outdoor dataset with manual annotated segmentation). To compensate for the absence of semantic annotations in KITTI, we generate segmentations using Detectron2 [51], employing the R101-FPN checkpoint trained on COCO panoptic segmentation data.

NYU includes 894 classes, and KITTI (with Detectron2 segmentation) has 133. We define underrepresented classes as those appearing in fewer than 10% of training images but occurring more than five times, enabling analysis of the long tail while preserving natural distributions. For NYU, there are 231 underrepresented classes, while for KITTI, we have 22. Interestingly, we find that these long-tail cases occur in 93% of test examples in NYU and 51% in KITTI.

For Cityscapes, we designate the following as underrepresented classes: truck, bus, caravan, trailer, and train, based on their substantially lower instance counts, roughly an order of magnitude fewer than more common categories. The test sets include 611 samples for NYU, 334 for KITTI, and 133 for Cityscapes. Notably, NYU contains a large number of sparsely represented classes, making it particularly well-suited for evaluating our task.

Metrics. We adopt standard depth estimation metrics [11], including threshold accuracy (δ_n), relative absolute error (RelAbs), root mean squared error (RMS), RMS in logarithmic space (RMS_{log}), and average Log₁₀ error (Log₁₀). Using these metrics, we conduct two types of evaluations: (1) underrepresented classes evaluation, where metrics are computed exclusively on pixels belonging to underrepresented semantic classes in the test images; and (2) all classes evaluation, where metrics are computed across all pixels in the test images, corresponding to the standard test set.

Baselines. We refer to our method as RAD-X, where X denotes the size of the ViT encoder. We compare it against two categories of baselines: fine-tuning and zero-shot approaches (other methods in Sec. 2 operate in different settings). In the fine-tuning category, we compare to BTS [30],

Table 1. **Underrepresented classes evaluation.** Comparison of depth estimation performance on **underrepresented classes** across NYU, KITTI, and Cityscapes datasets. Top: fine-tuning methods, middle: zero-shot methods, bottom: our method. \dagger : ZoeDepth is zero-shot for Cityscapes, but fine-tuned for NYU and KITTI. Best result in bold, second best underlined. Missing values correspond to methods without available code or trained model and that have not reported the relevant values in the literature.

Method	NYU						KITTI						Cityscapes					
	\uparrow			\downarrow			\uparrow			\downarrow			\uparrow			\downarrow		
	δ_1	δ_2	δ_3	AbsRel	RMS	Log ₁₀	δ_1	δ_2	δ_3	AbsRel	RMS	RMS _{log}	δ_1	δ_2	δ_3	AbsRel	RMS	RMS _{log}
AdaBins [2]	81.0	88.3	93.7	0.173	0.522	0.053	87.2	95.3	98.7	0.143	4.567	0.193	—	—	—	—	—	—
NewCRF [57]	80.3	89.7	95.4	0.169	0.497	0.049	89.1	96.7	99.1	0.121	4.247	0.166	—	—	—	—	—	—
DepthAnyV2 [53]	91.4	98.2	99.8	0.089	0.327	0.049	92.3	97.8	99.1	0.083	2.893	0.086	89.2	94.7	99.1	0.110	7.804	0.166
ZoeDepth \dagger [4]	90.9	98.1	99.6	0.098	0.334	0.043	88.6	96.9	98.4	0.116	3.908	0.140	40.9	66.7	79.3	0.314	17.051	0.496
DepthPro [5]	89.6	97.6	99.1	0.106	0.375	0.048	77.9	97.7	99.3	0.160	2.698	0.170	47.5	87.8	98.0	0.224	11.973	0.285
Metric3Dv2 [56]	92.4	97.6	99.4	0.095	0.331	0.039	89.8	97.7	99.4	0.121	<u>2.577</u>	0.141	<u>92.1</u>	97.1	98.5	0.097	7.063	<u>0.152</u>
UniDepthV2 [39]	92.8	98.1	99.3	0.092	0.329	0.039	90.5	98.2	99.4	0.111	4.059	0.130	88.3	96.4	98.2	0.136	7.777	0.171
RAD-Small	95.3	98.5	99.1	0.084	0.321	0.057	92.2	95.9	98.0	0.143	3.943	0.097	86.7	96.6	98.5	0.133	5.573	0.168
RAD-Base	96.7	<u>99.4</u>	<u>99.7</u>	<u>0.072</u>	<u>0.299</u>	0.053	<u>95.1</u>	97.6	98.8	0.084	3.107	0.088	88.5	96.9	<u>99.0</u>	0.127	<u>5.191</u>	0.158
RAD-Large	97.5	99.5	99.9	0.063	0.288	0.040	96.6	98.6	99.4	0.072	2.498	0.052	93.5	<u>97.0</u>	99.1	0.090	5.083	0.150

Table 2. **All classes evaluation.** Comparison of depth estimation performance on **all classes** across NYU, KITTI, and Cityscapes datasets. Top: fine-tuning methods, middle: zero-shot methods, bottom: our method. Bold indicates best (for δ columns: largest; for lower-is-better columns: smallest). Underline indicates second best. \dagger : ZoeDepth is zero-shot for Cityscapes, but fine-tuned for NYU and KITTI. Best result in bold, second best underlined. Missing values correspond to methods without available code or trained model and that have not reported the relevant values in the literature.

Method	NYU						KITTI						Cityscapes					
	\uparrow			\downarrow			\uparrow			\downarrow			\uparrow			\downarrow		
	δ_1	δ_2	δ_3	AbsRel	RMS	Log ₁₀	δ_1	δ_2	δ_3	AbsRel	RMS	RMS _{log}	δ_1	δ_2	δ_3	AbsRel	RMS	RMS _{log}
BTS [30]	88.5	97.8	99.4	0.109	0.391	0.046	96.2	99.4	99.8	0.056	2.430	0.089	—	—	—	—	—	—
AdaBins [2]	90.3	98.4	99.7	0.103	0.364	0.044	96.4	99.5	<u>99.9</u>	0.058	2.360	0.088	—	—	—	—	—	—
NewCRF [57]	92.1	99.1	99.8	0.095	0.333	0.040	97.4	<u>99.7</u>	<u>99.9</u>	0.052	2.129	0.079	—	—	—	—	—	—
IEBins [45]	93.6	99.2	99.8	0.087	0.314	0.038	97.1	99.6	<u>99.9</u>	0.050	2.011	0.075	—	—	—	—	—	—
iDisc [37]	93.8	99.2	99.8	0.086	0.313	0.037	97.5	<u>99.7</u>	<u>99.9</u>	0.050	2.070	0.077	—	—	—	—	—	—
DepthAnyV2 [53]	98.4	99.8	100	0.056	0.206	0.024	98.3	99.8	100	0.045	1.861	0.067	93.5	<u>98.4</u>	<u>99.4</u>	0.080	4.901	0.143
ZoeDepth \dagger [4]	95.1	99.4	<u>99.9</u>	0.077	0.282	0.033	97.1	99.6	99.9	0.054	2.281	0.082	51.1	73.3	82.2	0.292	12.182	0.474
DepthPro [5]	91.8	98.0	99.2	0.099	0.387	0.045	83.5	97.8	99.3	0.141	3.375	0.157	70.8	93.3	97.7	0.169	8.020	0.255
Metric3Dv2 [56]	98.9	99.8	100	<u>0.047</u>	<u>0.183</u>	0.020	<u>98.5</u>	99.8	100	0.044	1.990	<u>0.064</u>	94.9	98.0	98.8	0.087	5.404	0.161
UniDepthV2 [39]	98.8	99.8	100	0.046	0.180	0.020	98.9	99.8	<u>99.9</u>	0.037	1.710	0.061	87.0	97.7	98.8	0.175	5.948	0.206
RAD-Small	96.8	99.7	<u>99.9</u>	0.066	0.233	0.028	97.7	99.7	<u>99.9</u>	0.051	2.311	0.077	90.6	97.8	99.3	0.092	5.375	0.154
RAD-Base	98.0	<u>99.7</u>	100	0.056	0.211	<u>0.023</u>	98.1	99.8	100	0.046	1.913	0.070	92.1	98.3	<u>99.4</u>	0.081	4.980	<u>0.143</u>
RAD-Large	98.8	99.8	100	0.048	0.192	0.020	98.9	99.8	100	0.043	<u>1.801</u>	0.065	93.8	98.7	99.7	0.078	4.891	0.140

AdaBins [2], NewCRF [57], IEBins [45], iDisc [37], and DepthAnything v2 [53]; in the zero-shot category, we compare to ZoeDepth [4], DepthPro [5], Metric3D v2 [22], and UniDepth v2 [39], which represent the state-of-the-art for MMDE. See supplementary for further details.

4.2. Quantitative Evaluation

We compare RAD against other state-of-the-art methods, reporting results based on publicly available code and pre-trained models, or as documented in the literature.

Underrepresented classes evaluation. Tab. 1 presents quantitative comparison of depth estimation methods evaluated on underrepresented data from NYU, KITTI, and Cityscapes. For methods with multiple network sizes, we

report results for the most comparable to a large ViT (the best variant). Overall, our RAD-Large consistently achieves the strongest performance across benchmarks.

On NYU, RAD-Large achieves the highest overall performance, with relative improvements of 29.2% in AbsRel and 11.9% in RMS compared to the best-performing non-RAD method, DepthAnything v2, the foundation of our approach. Additionally, it achieves a 5.1% gain in δ_1 over UniDepthV2, which ranks second in that metric, excluding other RAD models. On KITTI, RAD-Large again leads, demonstrating relative improvements of 13.3% in RelAbs, 39.5% in RMS_{log}, and 4.7% in δ_1 over the best non-RAD method, DepthAnything v2. Similarly, on Cityscapes, RAD-Large delivers the strongest results, with relative im-

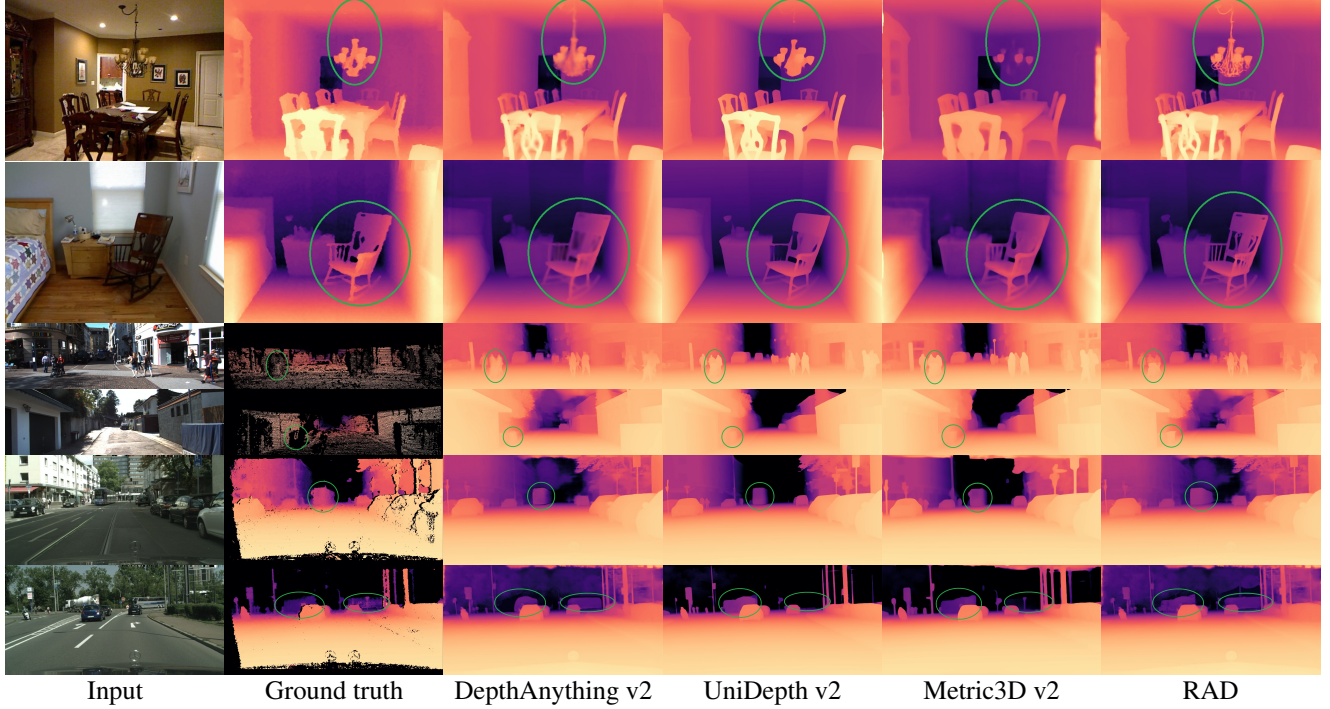


Figure 5. **Qualitative results** for NYU Depth v2 (top two rows), KITTI (middle two rows) and Cityscapes (bottom two rows). We compare our method (RAD) to baselines DepthAnything v2 [53], UniDepth v2 [39] and Metric3D v2 [22]. Best viewed zoomed in.

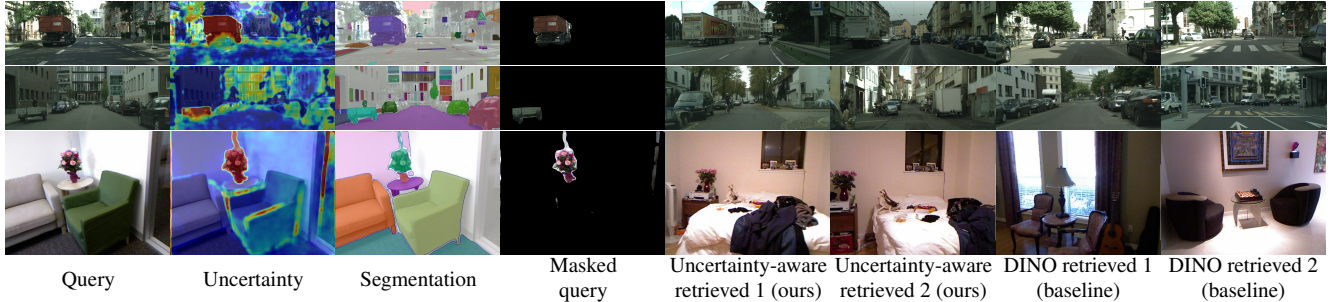


Figure 6. **Uncertainty-aware retrieval.** Comparison of image retrieval using our *uncertainty-aware* approach to the baseline *DINO*-based retrieval. Our approach identifies segments of high uncertainty in the query image and retrieves examples containing similar objects, rather than images with similar general layout. Best viewed zoomed in.

provements of 7.2% in AbsRel and 28.0% in RMS compared to Metric3Dv2, the best non-RAD baseline.

All classes evaluation. Tab. 2 presents a quantitative comparison to baselines evaluated across all semantic classes on NYU, KITTI, and Cityscapes, corresponding to the standard MMDE test protocol. On NYU and Cityscapes, RAD-Large performs on par with state-of-the-art methods such as UniDepthV2 and Metric3Dv2, while closely ranking second on KITTI. Notably, across all datasets, RAD-Large slightly outperforms DepthAnything v2, the backbone of our approach.

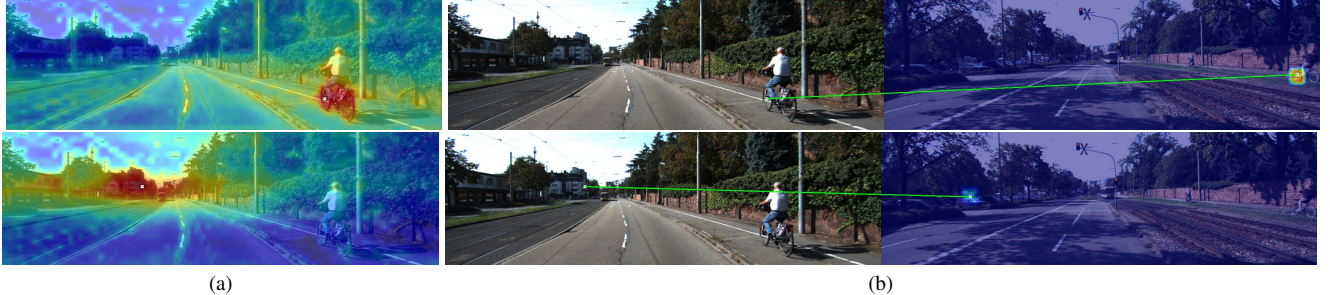
4.3. Qualitative Evaluation

Fig. 5 showcases qualitative results across the three datasets. RAD demonstrates a clear advantage in handling

underrepresented objects. Notably, DepthAnything v2 and RAD exhibit similar performance in in-domain regions of the image, a natural outcome given their shared backbone. RAD detects underrepresented elements with high uncertainty, delivering improved depth estimations in the lamp in the first image, the stroller in the third image, and the side of the train in the fifth image.

4.4. Component Visualization

Fig. 6 analyzes the uncertainty-aware image retrieval mechanism (Sec. 3.1.1). Uncertainty effectively localizes underrepresented classes. Combined with segmentation, it enables specific retrieval of context images containing visually similar object instances. In contrast, the baseline method, based on Nearest-Neighbour retrieval using global DINO



(a)

(b)

Figure 7. **Visualization of matched cross-attention.** For a selected patch in the input image, indicated by a white marker, and its corresponding matched point in the context image, we separately visualize the attention directed toward the input (a) and the context (b). When the match is correct, strong cross-attention emerges within the local neighborhood of the matched point in the context image. In contrast, incorrect matches yield weak cross-attention responses. Colormaps are kept consistent across images.

v2 [36] descriptors, tends to retrieve images with similar overall layouts and semantics but fails to capture the targeted underrepresented objects.

Fig. 7 illustrates matched cross-attention behavior (Sec. 3.1.3) by showing attention maps for input (a) and context (b) patches (all attention maps are computed by averaging across attention heads and ViT blocks). White markers denote reference patches; green lines show matches. The top row reflects a correct match, the bottom an incorrect one. In the input image, attention concentrates on semantically relevant regions for the selected patch (e.g., the bicycle). For a correct match, strong activation appears in the neighborhood of the matching location in the context image (e.g., the bicycle’s wheel), while incorrect matches result in weak attention responses, demonstrating the model’s ability to suppress unreliable correspondences, a direct consequence of our matching attention design. Additional examples are provided in the supplementary.

The supplementary material presents visualizations of point matching instances, showing that the method effectively identifies correspondences between visually similar underrepresented objects across diverse scenes.

Table 3. **Ablations** of RAD-Large, evaluated on Cityscapes.

Ablation	δ_1	AbsRel
RAD-Large	93.5	0.090
✗ 3D data augmentation in train	92.8	0.096
✗ Retrieved data in train	91.7	0.099
✗ Uncertainty-aware retrieval in train	91.9	0.102
✗ Uncertainty-aware retrieval in test	90.1	0.107
✗ Matched cross-attention	90.3	0.106
✗ Dual-stream (i.e., concat(in, retrieval))	89.4	0.109
✗ Retrieval (i.e., DepthAnyV2 [53])	89.2	0.110

4.5. Ablation Study

Our ablation study is conducted on the RAD-Large model, evaluated on the Cityscapes dataset. Table 3 confirms the necessity of all components. Removing *3D augmentation* or *retrieval* during training increases AbsRel by 6.7% and

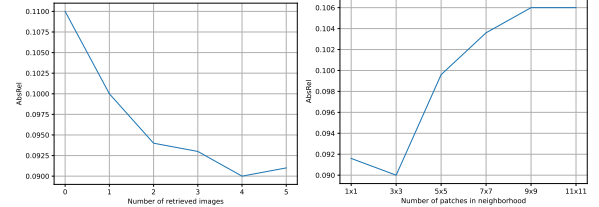


Figure 8. **Ablation on number of retrieved images and neighborhood size.** Absolute relative error as a function of the number of retrieved images (left) and neighborhood size in matched cross-attention (right) for RAD-Large, evaluated on Cityscapes.

10.0% respectively. The most critical component is the *uncertainty-aware retrieval*; disabling it (i.e. using global DINO KNN on the full image) at inference causes the largest drop (18.9% increase in AbsRel), confirming that targeted context is superior to global retrieval. Furthermore, replacing our *matched cross-attention* with standard full-context attention increases errors by 17.8%, validating the need for localized information transfer. Finally, eliminating the dual-stream design and instead using a single stream on the concatenated input and retrievals yields the worst performance, degrading AbsRel by over 22%.

We now examine a key parameter: the number of retrieved images. As shown in Fig. 8 (left), AbsRel steadily improves with more retrievals, reaching its lowest value at four. However, using five images introduces more irrelevant or misaligned content, slightly degrading performance.

Finally, we analyze the effect of neighborhood size in matched cross-attention. As shown in Fig. 8 (right), a 3×3 neighborhood yields optimal performance.

5. Conclusion

We presented RAD, a retrieval-augmented framework addressing the challenge of monocular depth estimation for underrepresented classes. By identifying regions of high uncertainty and retrieving semantically similar context, our method effectively supplements the network’s internal priors with external proxy geometric guidance. Through a dual-stream architecture and matched cross-attention, we

demonstrate that this targeted context can be reliably fused to correct depth in long-tail scenarios. Our approach achieves state-of-the-art performance on rare classes across NYUv2, KITTI, and Cityscapes, validating our approach.

References

- [1] Amir Atapour-Abarghouei and Toby P Breckon. Real-time monocular depth estimation using synthetic data with domain adaptation via image style transfer. In *Proceedings of the IEEE conference on computer vision and pattern recognition*, pages 2800–2810, 2018. [2](#)
- [2] Shariq Farooq Bhat, Ibraheem Alhashim, and Peter Wonka. Adabins: Depth estimation using adaptive bins. In *Proceedings of the IEEE/CVF conference on computer vision and pattern recognition*, pages 4009–4018, 2021. [1, 2, 6](#)
- [3] Shariq Farooq Bhat, Ibraheem Alhashim, and Peter Wonka. Localbins: Improving depth estimation by learning local distributions. In *European Conference on Computer Vision*, pages 480–496. Springer, 2022. [2](#)
- [4] Shariq Farooq Bhat, Reiner Birk, Diana Wofk, Peter Wonka, and Matthias Müller. Zoedepth: Zero-shot transfer by combining relative and metric depth. *arXiv preprint arXiv:2302.12288*, 2023. [1, 2, 6, 4](#)
- [5] Aleksei Bochkovskii, Amaël Delaunoy, Hugo Germain, Marcel Santos, Yichao Zhou, Stephan R. Richter, and Vladlen Koltun. Depth pro: Sharp monocular metric depth in less than a second. In *International Conference on Learning Representations*, 2025. [1, 2, 6](#)
- [6] Jun Cen, Peng Yun, Junhao Cai, Michael Yu Wang, and Ming Liu. Open-set 3d object detection. In *2021 International conference on 3D vision (3DV)*, pages 869–878. IEEE, 2021. [2](#)
- [7] Marius Cordts, Mohamed Omran, Sebastian Ramos, Timo Rehfeld, Markus Enzweiler, Rodrigo Benenson, Uwe Franke, Stefan Roth, and Bernt Schiele. The cityscapes dataset for semantic urban scene understanding. In *Proceedings of the IEEE conference on computer vision and pattern recognition*, pages 3213–3223, 2016. [2, 5](#)
- [8] Matthijs Douze, Alexandre Guzhva, Chengqi Deng, Jeff Johnson, Gergely Szilvassy, Pierre-Emmanuel Mazaré, Maria Lomeli, Lucas Hosseini, and Hervé Jégou. The faiss library. *IEEE Transactions on Big Data*, 2025. [4](#)
- [9] Ruofei Du, Eric Turner, Maksym Dzitsiuk, Luca Prasso, Ivo Duarte, Jason Dourgarian, Joao Afonso, Jose Pascoal, Josh Gladstone, Nuno Cruces, et al. Depthlab: Real-time 3d interaction with depth maps for mobile augmented reality. In *Proceedings of the 33rd Annual ACM Symposium on User Interface Software and Technology*, pages 829–843, 2020. [1](#)
- [10] Ainaz Eftekhari, Alexander Sax, Jitendra Malik, and Amir Zamir. Omnidata: A scalable pipeline for making multi-task mid-level vision datasets from 3d scans. In *Proceedings of the IEEE/CVF International Conference on Computer Vision*, pages 10786–10796, 2021. [2](#)
- [11] David Eigen, Christian Puhrsch, and Rob Fergus. Depth map prediction from a single image using a multi-scale deep network. *Advances in neural information processing systems*, 27, 2014. [2, 5, 3](#)
- [12] Sean Ryan Fanello, Cem Keskin, Shahram Izadi, Pushmeet Kohli, David Kim, David Sweeney, Antonio Criminisi, Jamie Shotton, Sing Bing Kang, and Tim Paek. Learning to be a depth camera for close-range human capture and interaction. *ACM Transactions on Graphics (TOG)*, 33(4):1–11, 2014. [1](#)
- [13] Huan Fu, Mingming Gong, Chaohui Wang, Kayhan Batmanghelich, and Dacheng Tao. Deep ordinal regression network for monocular depth estimation. In *Proceedings of the IEEE conference on computer vision and pattern recognition*, pages 2002–2011, 2018. [1, 2](#)
- [14] José M. Fácil, Alejo Concha, L. Montesano, and Javier Civera. Single-view and multiview depth fusion, 2016. [2](#)
- [15] Andreas Geiger, Philip Lenz, and Raquel Urtasun. Are we ready for autonomous driving? the kitti vision benchmark suite. In *2012 IEEE conference on computer vision and pattern recognition*, pages 3354–3361. IEEE, 2012. [2, 5](#)
- [16] Clément Godard, Oisin Mac Aodha, Michael Firman, and Gabriel J Brostow. Digging into self-supervised monocular depth estimation. In *Proceedings of the IEEE/CVF international conference on computer vision*, pages 3828–3838, 2019. [2](#)
- [17] Vitor Guizilini, Rares Ambrus, Sudeep Pillai, Allan Raventos, and Adrien Gaidon. 3d packing for self-supervised monocular depth estimation. In *Proceedings of the IEEE/CVF conference on computer vision and pattern recognition*, pages 2485–2494, 2020. [2](#)
- [18] Vitor Guizilini, Igor Vasiljevic, Dian Chen, Rareş Ambrus, and Adrien Gaidon. Towards zero-shot scale-aware monocular depth estimation. In *Proceedings of the IEEE/CVF International Conference on Computer Vision*, pages 9233–9243, 2023. [1, 2](#)
- [19] Zhuolin He, Xinrun Li, Heng Gao, Jiachen Tang, Shoumeng Qiu, Wenfu Wang, Lijian Lu, Xuchong Qiu, Xiangyang Xue, and Jian Pu. Towards open-set camera 3d object detection. *arXiv preprint arXiv:2406.17297*, 2024. [2](#)
- [20] Peter Hedman, Suhib Alsisan, Richard Szeliski, and Johannes Kopf. Casual 3d photography. *ACM Transactions on Graphics (TOG)*, 36(6):1–15, 2017. [1](#)
- [21] Julia Hornauer, Adrian Holzbock, and Vasileios Belagiannis. Out-of-distribution detection for monocular depth estimation. In *Proceedings of the IEEE/CVF International Conference on Computer Vision*, pages 1911–1921, 2023. [2](#)
- [22] Mu Hu, Wei Yin, Chi Zhang, Zhipeng Cai, Xiaoxiao Long, Hao Chen, Kaixuan Wang, Gang Yu, Chunhua Shen, and Shaojie Shen. Metric3d v2: A versatile monocular geometric foundation model for zero-shot metric depth and surface normal estimation. *IEEE Transactions on Pattern Analysis and Machine Intelligence*, 2024. [2, 6, 7](#)
- [23] Xuetong Hu, Ce Zhang, Yi Zhang, Bowen Hai, Ke Yu, and Zhihai He. Learning to adapt clip for few-shot monocular depth estimation. In *Proceedings of the IEEE/CVF Winter Conference on Applications of Computer Vision*, pages 5594–5603, 2024. [2](#)
- [24] Chengjie Huang, Vahdat Abdelzad, Christopher Gus Mannes, Luke Rowe, Benjamin Therien, Rick Salay, Krzysztof Czarnecki, et al. Out-of-distribution detection for

lidar-based 3d object detection. In *2022 IEEE 25th International Conference on Intelligent Transportation Systems (ITSC)*, pages 4265–4271. IEEE, 2022. 2

[25] Jiahui Huang, Zan Gojcic, Matan Atzmon, Or Litany, Sanja Fidler, and Francis Williams. Neural kernel surface reconstruction. In *Proceedings of the IEEE/CVF Conference on Computer Vision and Pattern Recognition*, pages 4369–4379, 2023. 1

[26] Kevin Karsch, Ce Liu, and Sing Bing Kang. Depth extraction from video using non-parametric sampling. In *European conference on computer vision*, pages 775–788. Springer, 2012. 2

[27] Bingxin Ke, Anton Obukhov, Shengyu Huang, Nando Metzger, Rodrigo Caye Daudt, and Konrad Schindler. Repurposing diffusion-based image generators for monocular depth estimation. In *Proceedings of the IEEE/CVF conference on computer vision and pattern recognition*, pages 9492–9502, 2024. 2

[28] Michael Kösel, Marcel Schreiber, Michael Ulrich, Claudius Gläser, and Klaus Dietmayer. Revisiting out-of-distribution detection in lidar-based 3d object detection. In *2024 IEEE Intelligent Vehicles Symposium (IV)*, pages 2806–2813. IEEE, 2024. 2

[29] Iro Laina, Christian Rupprecht, Vasileios Belagiannis, Federico Tombari, and Nassir Navab. Deeper depth prediction with fully convolutional residual networks. In *2016 Fourth international conference on 3D vision (3DV)*, pages 239–248. IEEE, 2016. 2

[30] Jin Han Lee, Myung-Kyu Han, Dong Wook Ko, and Il Hong Suh. From big to small: Multi-scale local planar guidance for monocular depth estimation. *arXiv preprint arXiv:1907.10326*, 2019. 5, 6

[31] Patrick Lewis, Ethan Perez, Aleksandra Piktus, Fabio Petroni, Vladimir Karpukhin, Naman Goyal, Heinrich Küttler, Mike Lewis, Wen-tau Yih, Tim Rocktäschel, et al. Retrieval-augmented generation for knowledge-intensive nlp tasks. *Advances in neural information processing systems*, 33:9459–9474, 2020. 2

[32] Rui Li, Dong Gong, Wei Yin, H. Chen, Yu Zhu, Kaixuan Wang, Xiaozhi Chen, Jinqiu Sun, and Yanning Zhang. Learning to fuse monocular and multi-view cues for multi-frame depth estimation in dynamic scenes, 2023. 2

[33] Philipp Lindenberger, Paul-Edouard Sarlin, and Marc Pollefeys. Lightglue: Local feature matching at light speed. In *Proceedings of the IEEE/CVF international conference on computer vision*, pages 17627–17638, 2023. 4, 2, 5

[34] Adrian Lopez-Rodriguez and Krystian Mikolajczyk. Desc: Domain adaptation for depth estimation via semantic consistency. *International Journal of Computer Vision*, 131(3):752–771, 2023. 2

[35] Mircea Paul Muresan, Marchis Raul, S. Nedevschi, and R. Danescu. Stereo and mono depth estimation fusion for an improved and fault tolerant 3d reconstruction, 2021. 2

[36] Maxime Oquab, Timothée Darcet, Théo Moutakanni, Huy Vo, Marc Szafraniec, Vasil Khalidov, Pierre Fernandez, Daniel Haziza, Francisco Massa, Alaaeldin El-Nouby, et al. Dinov2: Learning robust visual features without supervision. *arXiv preprint arXiv:2304.07193*, 2023. 4, 8

[37] Luigi Piccinelli, Christos Sakaridis, and Fisher Yu. idisc: Internal discretization for monocular depth estimation. In *Proceedings of the IEEE/CVF Conference on Computer Vision and Pattern Recognition*, pages 21477–21487, 2023. 6

[38] Luigi Piccinelli, Yung-Hsu Yang, Christos Sakaridis, Mattia Segu, Siyuan Li, Luc Van Gool, and Fisher Yu. Unidepth: Universal monocular metric depth estimation. In *Proceedings of the IEEE/CVF Conference on Computer Vision and Pattern Recognition*, pages 10106–10116, 2024. 2

[39] Luigi Piccinelli, Christos Sakaridis, Yung-Hsu Yang, Mattia Segu, Siyuan Li, Wim Abbeloos, and Luc Van Gool. UniDepthV2: Universal monocular metric depth estimation made simpler. *arXiv preprint arXiv:2502.20110*, 2025. 1, 2, 6, 7

[40] Sudeep Pillai, Rareş Ambruş, and Adrien Gaidon. Superdepth: Self-supervised, super-resolved monocular depth estimation. In *2019 International Conference on Robotics and Automation (ICRA)*, pages 9250–9256. IEEE, 2019. 2

[41] Matteo Poggi, Filippo Aleotti, Fabio Tosi, and Stefano Maticoccia. On the uncertainty of self-supervised monocular depth estimation. In *Proceedings of the IEEE/CVF conference on computer vision and pattern recognition*, pages 3227–3237, 2020. 3

[42] René Ranftl, Katrin Lasinger, David Hafner, Konrad Schindler, and Vladlen Koltun. Towards robust monocular depth estimation: Mixing datasets for zero-shot cross-dataset transfer. *IEEE transactions on pattern analysis and machine intelligence*, 44(3):1623–1637, 2020. 2

[43] René Ranftl, Alexey Bochkovskiy, and Vladlen Koltun. Vision transformers for dense prediction. In *Proceedings of the IEEE/CVF international conference on computer vision*, pages 12179–12188, 2021. 2, 4, 1

[44] Nikhila Ravi, Valentin Gabeur, Yuan-Ting Hu, Ronghang Hu, Chaitanya Ryali, Tengyu Ma, Haitham Khedr, Roman Rädle, Chloe Rolland, Laura Gustafson, et al. Sam 2: Segment anything in images and videos. *arXiv preprint arXiv:2408.00714*, 2024. 3, 5

[45] Shuwei Shao, Zhongcai Pei, Xingming Wu, Zhong Liu, Weihai Chen, and Zhengguo Li. Iebins: Iterative elastic bins for monocular depth estimation. *Advances in Neural Information Processing Systems*, 36:53025–53037, 2023. 1, 2, 6

[46] Nathan Silberman, Derek Hoiem, Pushmeet Kohli, and Rob Fergus. Indoor segmentation and support inference from rgbd images. In *European conference on computer vision*, pages 746–760. Springer, 2012. 2, 5

[47] Louis Soum-Fontez, Jean-Emmanuel Deschaud, and François Goulette. Hd-ood3d: Supervised and unsupervised out-of-distribution object detection in lidar data. *arXiv preprint arXiv:2410.23767*, 2024. 2

[48] Lokesh Veeramacheneni and Matias Valdenegro-Toro. A benchmark for out of distribution detection in point cloud 3d semantic segmentation. *arXiv preprint arXiv:2211.06241*, 2022. 2

[49] Ruoyu Wang, Zehao Yu, and Shenghua Gao. Planedepth: Self-supervised depth estimation via orthogonal planes. In *Proceedings of the IEEE/CVF conference on computer vision and pattern recognition*, pages 21425–21434, 2023. 2

[50] Yan Wang, Wei-Lun Chao, Divyansh Garg, Bharath Hariharan, Mark Campbell, and Kilian Q Weinberger. Pseudolidar from visual depth estimation: Bridging the gap in 3d object detection for autonomous driving. In *Proceedings of the IEEE/CVF conference on computer vision and pattern recognition*, pages 8445–8453, 2019. 1

[51] Yuxin Wu, Alexander Kirillov, Francisco Massa, Wan-Yen Lo, and Ross Girshick. Detectron2. <https://github.com/facebookresearch/detectron2>, 2019. 5

[52] Jiaxin Xie, Chenyang Lei, Zhuwen Li, Li Erran Li, and Qifeng Chen. Video depth estimation by fusing flow-to-depth proposals, 2019. 2

[53] Lihe Yang, Bingyi Kang, Zilong Huang, Zhen Zhao, Xiaogang Xu, Jiashi Feng, and Hengshuang Zhao. Depth anything v2. *Advances in Neural Information Processing Systems*, 37:21875–21911, 2024. 1, 2, 3, 4, 6, 7, 8, 5

[54] Yung-Hsu Yang, Luigi Piccinelli, Mattia Segu, Siyuan Li, Rui Huang, Yuqian Fu, Marc Pollefeys, Hermann Blum, and Zuria Bauer. 3d-mood: Lifting 2d to 3d for monocular open-set object detection. *arXiv preprint arXiv:2507.23567*, 2025. 2

[55] Wei Yin, Jianming Zhang, Oliver Wang, Simon Niklaus, Long Mai, Simon Chen, and Chunhua Shen. Learning to recover 3d scene shape from a single image. In *Proceedings of the IEEE/CVF conference on computer vision and pattern recognition*, pages 204–213, 2021. 2

[56] Wei Yin, Chi Zhang, Hao Chen, Zhipeng Cai, Gang Yu, Kaixuan Wang, Xiaozhi Chen, and Chunhua Shen. Metric3d: Towards zero-shot metric 3d prediction from a single image. In *Proceedings of the IEEE/CVF international conference on computer vision*, pages 9043–9053, 2023. 2, 6

[57] Weihao Yuan, Xiaodong Gu, Zuozhuo Dai, Siyu Zhu, and Ping Tan. Neural window fully-connected crfs for monocular depth estimation. In *Proceedings of the IEEE/CVF conference on computer vision and pattern recognition*, pages 3916–3925, 2022. 1, 2, 6

[58] Yuheng Zhang, Mengfei Duan, Kunyu Peng, Yuhang Wang, Ruiping Liu, Fei Teng, Kai Luo, Zhiyong Li, and Kailun Yang. Out-of-distribution semantic occupancy prediction. *arXiv preprint arXiv:2506.21185*, 2025. 2

[59] Shanshan Zhao, Huan Fu, Mingming Gong, and Dacheng Tao. Geometry-aware symmetric domain adaptation for monocular depth estimation. In *Proceedings of the IEEE/CVF Conference on Computer Vision and Pattern Recognition*, pages 9788–9798, 2019. 2

[60] Tinghui Zhou, Matthew Brown, Noah Snavely, and David G Lowe. Unsupervised learning of depth and ego-motion from video. In *Proceedings of the IEEE conference on computer vision and pattern recognition*, pages 1851–1858, 2017. 2

RAD: Retrieval-Augmented Monocular Metric Depth Estimation for Underrepresented Classes

Supplementary Material

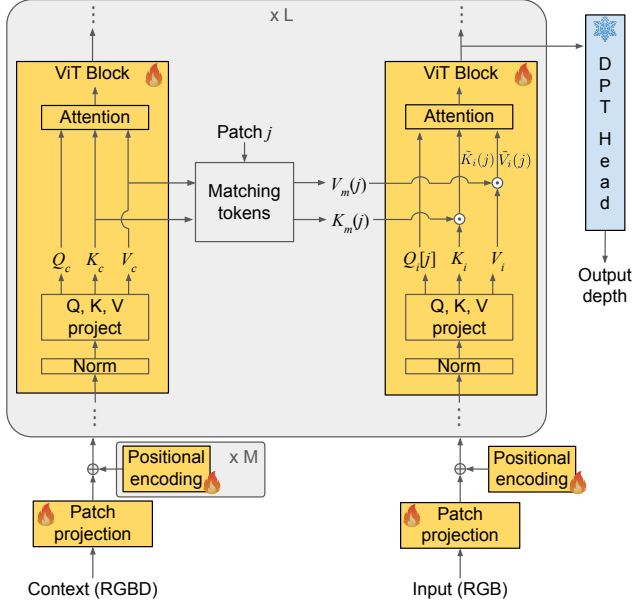


Figure 9. **Full network architecture.** The matched cross-attention mechanism allows the input stream to pull information from the context at the matched locations. Yellow blocks are optimized during training, while the blue block is frozen. Plus signs correspond to addition, the “dot” operation is concatenation.

A. Overall Network Architecture

Fig. 9 illustrates the complete network architecture employed in RAD. The design is based on the DepthAnything v2 framework [53], with one key modification: the original attention module is replaced by our matched cross-attention mechanism, which connects between the context and input streams. The remainder of the encoder’s Vision Transformer (ViT) architecture remains unchanged.

The system comprises a dual-stream encoder, which is trainable during optimization, and a frozen DPT head [43]. For each token j in the input stream, the *matching tokens* block retrieves matched keys $K_m(j)$ and values $V_m(j)$, derived from the context keys K_c and values V_c at corresponding matching positions. These matched representations are concatenated with the input keys K_i and values V_i , forming the input to the standard scaled dot-product attention mechanism within the ViT. The input and context queries, $Q_i[j]$ and Q_c , are processed following the original DepthAnything v2 approach.

Importantly, each stream employs its own *positional encoding*, enabling the encoder to distinguish between context

and input tokens. Additionally, each retrieved image is assigned a unique positional encoding, allowing the tokens to remain distinguishable within the upstream blocks of the ViT. Consequently, if M context samples are retrieved, the context stream utilizes M distinct positional encodings. All positional encoders are trainable to support this differentiation.

The *patch projection* for the input stream follows the original design of the DepthAnything v2 network. For the context stream, we introduce a fourth channel to process the sample’s depth, as detailed in Sec. 3.1.3. The procedures for *normalization* and *Q, K, V projection* are identical to those employed in each ViT block of DepthAnything v2. Similarly, the *attention* mechanism remains unchanged, utilizing scaled dot-product attention.

B. Additional Qualitative Results

Additional qualitative results are presented in Fig. 10.

C. Mesh Creation for 3D Augmentation

During training, context samples may be generated through 3D augmentation (Sec. 3.1.1). In this process, the input image is rendered from a novel viewpoint using ground-truth depth and camera calibration parameters. A straightforward approach is to back-project each pixel into 3D and re-project it onto a new image plane; however, this often produces large regions without valid signal because the new viewpoint is misaligned with the original pixel grid. Such gaps degrade the realism of augmented samples and can negatively impact downstream learning.

To address this limitation, we reconstruct a continuous surface mesh from the back-projected 3D point cloud, enabling dense coverage and improved geometric consistency. For mesh generation, we employ NCSR [25], which has demonstrated strong performance across multiple domains. Figure 11 compares image re-projection using only the point cloud versus the full mesh, highlighting the substantial improvement in completeness and fidelity.

D. Additional Component Visualizations

D.1. Point Matching

Fig. 12 demonstrates the performance of the point-matching algorithm on three representative input images containing underrepresented classes (left) and their corresponding retrieved images (right) from Cityscapes. While point-matching methods are typically trained on multiple views

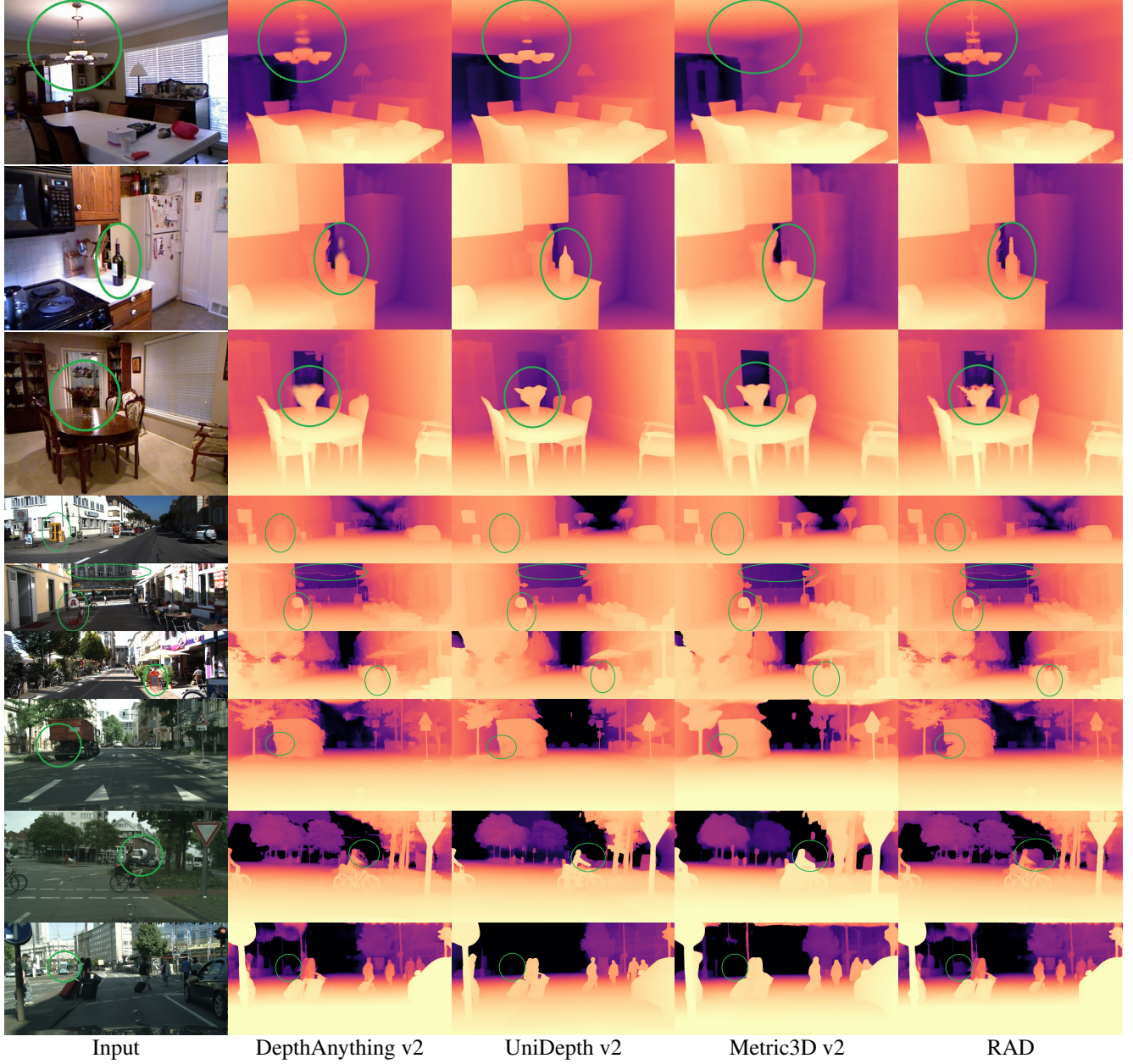


Figure 10. **Qualitative results** for NYU Depth v2 (top three rows), KITTI (middle three rows) and Cityscapes (bottom three rows). We compare our method (RAD) to baselines DepthAnything v2 [53], UniDepth v2 [39] and Metric3D v2 [22]. Best viewed zoomed in.

of the same scene, LightGlue [33] exhibits strong generalization to semantic similarities across different scenes, even under variations in scale and illumination. Notably, most matches occur on underrepresented objects, as these elements tend to be the most visually similar due to the uncertainty-aware retrieval mechanism described in Sec. 3.1.1.

D.2. Matched cross-attention

Fig. 13 illustrates additional results for matched cross-attention. Attention to input patches consistently concentrates on relevant geometric structures, whereas attention to context patches is pronounced when point correspondences are correct and markedly weaker when correspondences are incorrect. This behavior underscores the model’s ability to leverage accurate matches for contextual reasoning, while reducing reliance on erroneous correspondences, thereby

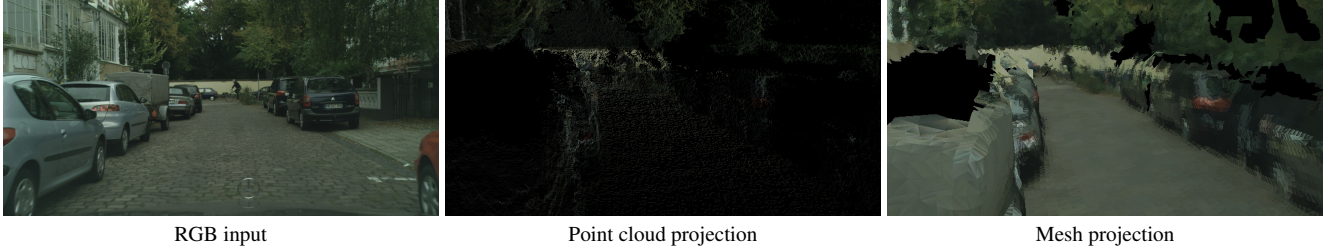


Figure 11. **Mesh creation for 3D augmentation.** The input image (left) is projected from a new point of view. When using only the point cloud defined by the image pixels, projection yields large unmeasured regions (middle). When a mesh is used to reconstruct geometry, the scene is densely reconstructed.



Figure 12. **Point matches for underrepresented classes** (top: tram, middle: truck, bottom: bus). The left image is sampled from the validation set, while the right image is from the training set. Matches remain consistent despite variations in illumination and scale.

enhancing robustness.

E. Training and Implementation Details

E.1. Network Optimization

Our training procedure was carried out in stages, as outlined below:

1. Start with pre-trained DepthAnything v2.
2. Fine-tune the DepthAnything v2 network on the training dataset to produce metric depth rather than relative depth. All weights are trained, with a significantly lower learning rate applied to the encoder, as recommended by the original authors.

3. Construct the context stream encoder by duplicating the fine-tuned encoder from Step 2. Modify the projection operation in the context ViT encoder to accept the depth channel (Sec. 3.1.3 in the main paper).

4. Freeze the decoder and fine-tune the dual-stream encoder. Optimization is performed on the training dataset using the complete retrieval-augmented pipeline (Sec. 3.1.1 in the main paper).

In Step 4 we optimized the positional encoding in both streams so that the network learns to differentiate between the two types of inputs.

As objective, we used the scale invariant log loss [11], also used by DepthAnything v2. We trained our models

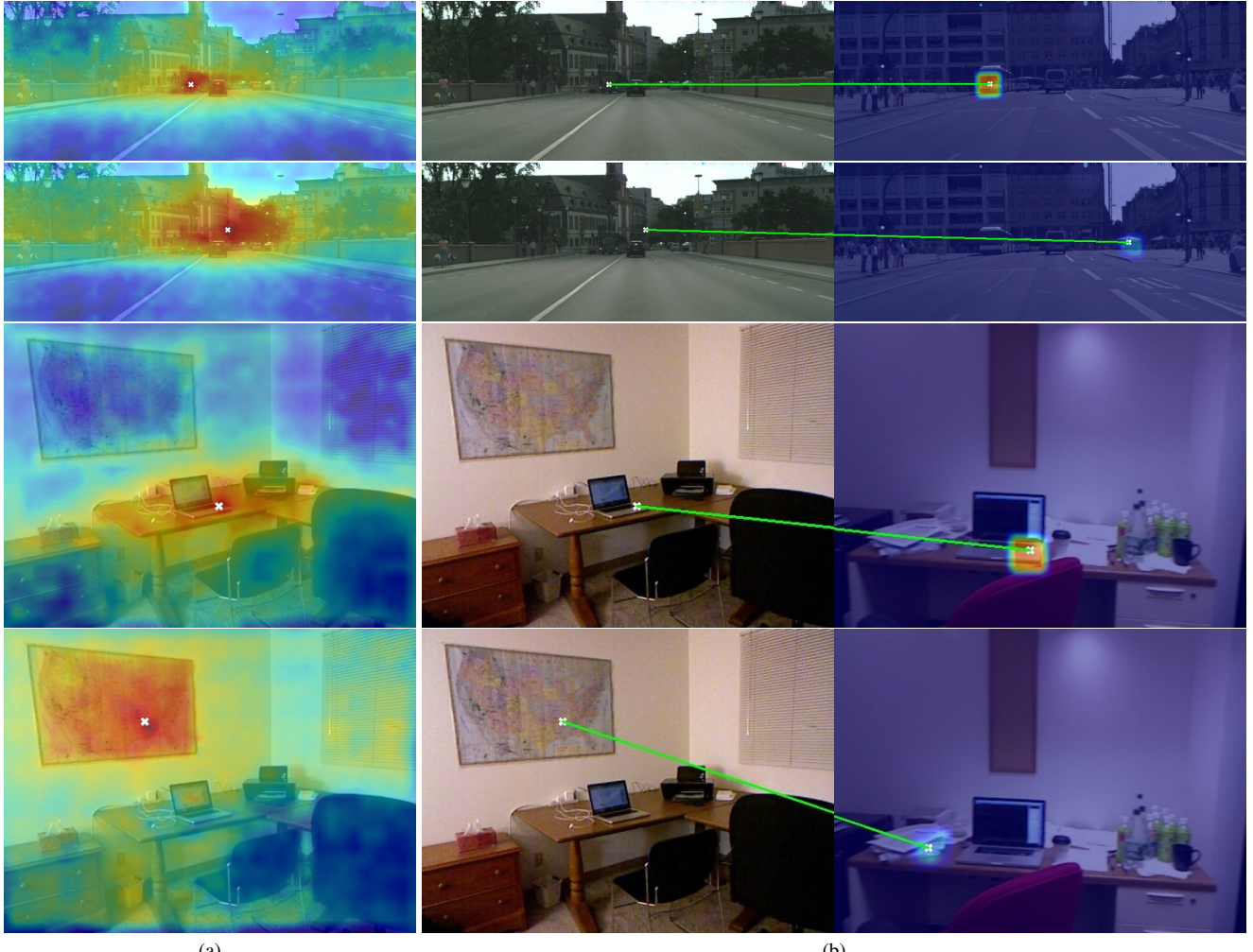


Figure 13. **Visualization of matched cross-attention.** For a selected patch in the input image, indicated by a white marker, and its corresponding matched point in the context image, we separately visualize the attention directed toward the input (a) and the context (b). When the match is correct, strong cross-attention emerges within the local neighborhood of the matched point in the context image. In contrast, incorrect matches yield weak cross-attention responses. Colormaps are kept consistent across images.

using the AdamW optimizer with $\beta_1 = 0.9$, $\beta_2 = 0.999$, and a weight decay of 1×10^{-2} . The initial learning rate was set to 5×10^{-5} and decayed by a factor of 10 after 5 epochs of stagnation. Training was performed on four Nvidia L40S GPUs.

E.2. Uncertainty-aware Image Retrieval

To compute uncertainty, we generated 5 noisy variants of a given image by adding Gaussian noise with a standard deviation $\sigma = 0.1$ (for normalized image values). The parameters h and q in Section 3.1.1 were set to 0.05 and 20%, respectively. Unless explicitly stated otherwise, in the experiments (Sec. 4) we retrieved 4 images and applied matched cross-attention using a 3×3 patch neighborhood. To perform efficient search we use the FAISS library [8].

E.3. Baseline Details

For each baseline in the experiments section (Sec. 4) we use the publicly available code and weights. Specifically, for ZoeDepth [4] we use the horizontal flip augmentation suggested by the authors. All methods are run according to their official instructions.

F. Runtime and Memory Analysis

We evaluate the model size, memory footprint, and inference runtime of RAD, and compare these metrics against those of the baseline architecture, DepthAnything v2 [53], as presented in Tab. 4. All measurements are conducted on Cityscapes images at a resolution of 2048×1024 , using a single Nvidia L40S GPU and a RAD configuration that in-

corporates four context samples.

Table 4. Parameter count, memory and runtime analysis. Compared to DepthAnything v2 [53], RAD has approximately twice the parameter count and memory due to the second stream. Runtime is in seconds.

Method	Parameters	Memory	Runtime
DepthAny-Small	24.8M	94.55 MB	0.013 s
DepthAny-Base	97.5M	371.82 MB	0.017 s
DepthAny-Large	335.3M	1279.13 MB	0.019 s
RAD-Small	48.5M	184.99 MB	1.724 s
RAD-Base	187.4M	714.72 MB	1.738 s
RAD-Large	644.1M	2457.02 MB	1.780 s

Table 5. Runtime breakdown for RAD-Large. All values are reported in seconds.

Process	RAD-Small	RAD-Base	RAD-Large
Uncertainty	0.017 s	0.020 s	0.024 s
Segmentation	1.487 s	1.487 s	1.487 s
Point matching	0.191 s	0.191 s	0.191 s
KNN search	0.015 s	0.015 s	0.015 s
Feed-forward	0.014 s	0.025 s	0.063 s

A detailed breakdown of RAD’s runtime is provided in Tab. 5. To estimate uncertainty, five inference operations are executed in parallel, corresponding to five noisy versions of the input image. Similarly, the four context samples and the input image are processed concurrently during RAD’s feed-forward pass, synchronizing only to exchange information for matched cross-attention.

For RAD, both the parameter count and memory consumption are approximately doubled relative to DepthAnything v2, primarily due to the inclusion of the context stream. The inference time is substantially higher, rendering RAD unsuitable for real-time applications. This increase in runtime is largely attributable to the SAM2 segmentation [44] and LightGlue point matching [33] procedures. Consequently, the proposed approach would benefit significantly from future advances in segmentation and point-matching frameworks that combine accuracy with computational efficiency. Furthermore, it is possible to adapt the method to real-time applications by removing the segmentation process, and using only uncertainty, yielding a bit more noisy retrieval but improved runtime.

G. Limitations

RAD exhibits three primary limitations:

1. **High runtime.** The method’s inference time is prohibitively large for real-time applications, with most of

the overhead arising from image segmentation used for uncertainty-aware retrieval. A potential alternative is to employ pixel-wise uncertainty without coupling it to segmentation, enabling faster retrieval at the cost of increased noise, a trade-off that may be acceptable for real-time scenarios.

2. **Dependence on depth-annotated context data.** RAD requires a context dataset with ground-truth depth, which is not always available. While the context stream could operate on RGB-only inputs and leverage proxy multi-view cues to improve depth estimation, ground-truth depth is a strong signal for accurate performance.
3. **Sensitivity to retrieval and matching errors.** The approach relies on accurate image retrieval and point matching, as these components feed the matched cross-attention mechanism. Although attention partially mitigates this issue by down-weighting unreliable patches, errors in these stages can still propagate and degrade overall performance.